Research Project: RAM-Air Parachute Real Time Piloting Simulator

Student: Tamar Alperin
Advisor: Dr. Anna Clarke
Technion - Israel Institute of Technology, Haifa 3200003, Israel

RAM Air parachutes are commonly used for military purposes, precision delivery systems, and sports skydiving. RAM Air parachutes can be considered low aspect ratio wings; thus, they are highly maneuverable and very challenging to control. Achieving a high or even adequate skill level in piloting requires an extensive amount of training. However, conventional piloting training can only provide theoretical knowledge, while the required capabilities are acquired from trial and error in the sky. In a field where safety is of high importance and an error can be fatal, it is beneficial for both piloting students and professionals to have an available simulator for training on the ground. Therefore, the goal of this project is to develop a parafoil piloting real-time simulator to provide a training environment for pilots. We will implement a 6-DOF (Degrees Of Freedom) dynamic model that considers the parafoil and pilot as a rigid body, and a high-fidelity 9-DOF model that accounts for payload rotation in reference to the canopy. Additionally, we will introduce the developed real-time user interactive simulation and compare the results with our expectations.

1 Introduction

The overall goal of the study is to develop a parafoil piloting simulator to provide a training environment for parafoil pilots. The project is a part of a larger effort to develop the said simulator, which includes a physical interface, testing methods, pilot group interaction simulation, and wind modeling. In this project, we will only focus on the real-time dynamic simulation. This report will discuss the implementation of a dynamic model of a RAM Air Parachute during flight and landing. A RAM Air parachute is a parafoil, a non-rigid airfoil with an aerodynamic cell structure that is inflated by the wind [1]. Unlike traditional round parachutes, RAM Air parachutes are controllable. The control is provided by steering lines attached to the parafoil. The dynamic model will only apply to the stages of the flight where the parachute is fully inflated. At these stages, the parafoil can be described as a low aspect ratio wing. First, we will provide an overview of existing simulation methods and state the methods we have chosen. Then, we will explain in detail the dynamic models relevant to the problem and formulate the equations of motion. Next, we will describe in depth the components of the developed simulator. Finally, we will analyze the simulation results and compare them

with expectations based on physical laws.

2 Literature Survey

The piloting simulator we want to develop is a system that provides real-time continuous data about the position and orientation of both the parafoil and the payload. To develop the simulator, the equations of motion must be formulated in a way that best describes the principal dynamics of the parafoil. Then the equations of motion shall be solved numerically in real time to give the user continuous feedback on the position and orientation of the parafoil.
Developing a dynamic model requires substituting the aerodynamic forces into the equations of motion. There are two main approaches described in the literature for obtaining the aerodynamic forces.

Numerical approach for obtaining aerodynamic forces

The first approach uses computational fluid dynamics (CFD) to calculate the flow field around the parafoil. In this method, numerical tools are used for solving the fluid dynamics equations, mainly Navier-Stokes equations, and for computing the aerodynamic forces [1, 2]. Various CFD tools are used to compute 2D/3D flow fields given different properties such as parafoil dimensions, angle of attack, wind gusts, etc. Due to complexity of the geometry and the aerodynamics of the parafoil, it is beneficial to use CFD to generate accurate aerodynamic models. However, it is mentioned in the literature that performing full CFD computations for a large geometry like a RAM Air parachute requires extensive computing resources. Hence, it is impossible to perform these calculations in real time. A different option is to compute the flow field in various scenarios and to collect a pool of data containing the aerodynamic forces received from a given set of conditions, i.e., a certain angle of attack, certain wind speed, etc. Then, it can be possible to interpolate the data in real time during the simulation to receive the approximated aerodynamic forces at each instance of time. The accuracy of the interpolation depends on the amount and the variety of the data collected. Hence, the high accuracy of the numeric computation does not guarantee a highly accurate aerodynamic model. Moreover, substantial resources are required to conduct all the essential computations necessary for gathering the data pool.

Analytical approach for obtaining aerodynamic forces

The second approach consists of implementing approximated models of the aerodynamic forces to the equations of motion using experimental-based aerodynamic coefficients [3]. A detailed description of several experiments performed to obtain aerodynamic coefficients can be found in [4].
The analytic approach is more suitable for obtaining the aerodynamic forces since it does not require high-performance computing resources and thus it is possible to create a real-time simulation. The models can still provide sufficient

accuracy for simulating the real forces applied during flight. Nevertheless, the analytic approach also has a few limitations; for example, it does not consider the effects of turbulence on the motion.

Dynamic models

There are various dynamic models described in the literature, from simplified 3-DOF models to more complex 9-DOF models. The more simplified models with less than 6-DOF neglect some of the translation and rotation degrees of freedom. The next level of complexity is 6-DOF models in which the parafoil and payload are considered a rigid body. The most complex 9-DOF models allow the payload to rotate freely with respect to the parafoil. A detailed comparison between the models can be found in [5]. The vast majority of models described in the literature that have more than 6-DOF are multi-body models. That is, the parafoil and the payload are considered different bodies, each with its own DOF. The number of DOF is determined by the connection between the payload and the parafoil. For example, four rigid links connecting each of the payload's corners to each of the parafoil's corners with pin joints can be modeled using only 7-DOF: 6-DOF for the rotation and translation of the parafoil and payload together, and 1-DOF for the relative rotation of the payload around the pitch axis with respect to the parafoil [3, 6]. The different connection points can be seen in Fig. 1.

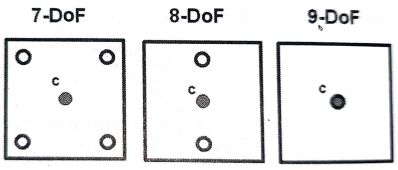

Fig. 1 Payload connection points [3]

There are several articles that take the analytic approach for calculating the aerodynamic forces, and use them to implement a dynamic model of a parafoil. We chose to focus on two main papers [7, 8]. Similar models from the literature can be found in [5, 6, 9] and in the book by O. Yakimenko [3].

In [7] a real-time 6-DOF computational model is developed to simulate the parafoil's dynamics. The aerodynamic forces are calculated using the known equations for wings. The 6-DOF model is solved using fourth-order Runge-Kutta to obtain the position, orientation, velocity, and angular rates of the parafoil. Those states are then fed back to the dynamic model to compute the following step. In addition, external steering inputs in the form of trailing edge deflection are added to the system. The study also considers the effect of apparent mass, which is the motion of a certain amount of fluid mass caused by the motion of the parafoil through the air (see Sec. 3.1). As mentioned previously, the analytic approach to calculating the aerodynamic forces does not require extensive computing resources, and was used in this article to develop a real-time simulation.

In [8] a 6-DOF model is developed using conventional theories for wings, adapted to a low aspect ratio wing with

anhedral angle. The study describes the relation between the aerodynamic coefficients, the angle of attack, the aspect ratio, and the anhedral angle. Moreover, in the study, a direction stabilization system is developed to control the parafoil's attitude. The model is implemented in Matlab Simulink and the performance of the control system is tested under various conditions.

Based on the literature review presented above, we started by implementing a 6-DOF model that considers the parafoil and payload as a rigid body, similar to what was done in [7]. The system receives the environmental conditions and the steering input, and presents the position and orientation of the parafoil in the 3D environment, as well as the parafoil's velocity and angular rates at each instant of time. The dynamic model and the aerodynamic coefficients were taken from the book by O. Yakimenko [3]. The overall 6-DOF and 9-DOF models are described in detail in the following sections, along with the simulation results.

3 Parafoil Dynamics Models

In this project we aim to implement two models that describe the dynamics of the parafoil: A 6-DOF model, and a high fidelity 9-DOF model. In this chapter we will discuss the two models and explain them in detail. Implementing these models requires a large number of coefficients that describe the parafoil, from physical properties such as mass and moment of inertia, to aerodynamic coefficients that are needed to calculate the aerodynamic forces and moments based on the state of the parafoil. Since it is hard to obtain reliable data, we chose to use the data provided by O.Yakimenko in [3]. The data belongs to a small PADS (Precision Aerial Delivery System) called "SnowFlake", with a surface of $1[m^2]$ and a weight of a few kilograms. Although it is different from the larger parafoils used by pilots, we preferred using reliable and available data for the initial model. All the properties used can be found in the simulator code.

Before we dive into the models, it is important to understand the affect of apparent mass and its significance to the dynamics of the system.

3.1 Apparent mass

When a body moves inside a fluid, it pushes the fluid, and causes it to move. The moved fluid applies pressure on the moving body, called "Apparent mass pressure". In our case, the parafoil moves through the air, therefore, the air applies pressure on the parafoil. One way of estimating the significance of the apparent mass effect is by wing loading. The apparent mass is significant when the wing loading is smaller that $5[\frac{kg}{m^2}]$ [10]. For the "SnowFlake", the wing loading is $2.5[\frac{kg}{m^2}]$ [table 5.3 in [3]]. Hence, apparent mass has to be considered. Another way is based on the mass ratio of the parafoil. The Mass ratio equals the mass of the payload (in our case, pilot) divided by the mass displaced by the parafoil, as can be seen in Eq. (1), where S is the parafoil area, and ρ is the density of the fluid (in our case, air). In the case of ram air parachutes we roughly assume a cubic shape, hence $V = S^{\frac{3}{2}}$.

$$M_r = \frac{m_{payload}}{m_a} = \frac{m_{payload}}{\rho S^{\frac{3}{2}}} \tag{1}$$

For lower M_r we receive higher apparent mass pressure. For a parafoil, M_r is significantly lower than for an aircraft, where the apparent mass effect is negligible. For the "Snowflake", we receive $M_r = 2.5$ [table 5.3 in [3]], which is considered very small, especially compared to an aircraft. Hence, we should take apparent mass into consideration in our dynamic model.

Note, that the apparent mass does not equal the mass of the air displaced by the parafoil. However, the apparent mass is a way to represent the extra force caused by the "apparent mass pressure" as an extra mass added to the parafoil system. Therefore, we can define a center of apparent mass, which is different from the center of mass of the parafoil + payload. The added apparent mass has a moment of inertia that adds to the inertia of the body. The apparent mass and inertia matrices are diagonal, as can be seen in Eq. (2), Eq. (3). The values A, B, C, I_A, I_B, I_C are determined by the geometry of the parafoil, and can be obtained by different methods. For example, by presenting the parafoil as cylinders or as rectangular cuboids. In this project we relied on the values presented as part of the properties of the parafoil.

$$I_{a.m} = \begin{bmatrix} A & 0 & 0 \\ 0 & B & 0 \\ 0 & 0 & C \end{bmatrix} \tag{2}$$

$$I_{a.i} = \begin{bmatrix} I_A & 0 & 0 \\ 0 & I_B & 0 \\ 0 & 0 & I_C \end{bmatrix} \tag{3}$$

The corresponding forces and moments can be obtained using Newtons second law in the parafoil frame, whose origin is the center of apparent mass. The vector between the parafoil's center of mass and the center of apparent mass is called $\bar{r}_{BM}$, and it is also needed, since the equations of motion are solved in body frame and not in parafoil frame. The full equations in body frame can be found in the "Equations of motion" section 3.2.4.

3.2 6-DOF Model

At first, we developed a 6-DOF model for the parafoil-pilot system. The six degrees of freedom are translations along 3 axes and rotations around 3 axes. In this model the parafoil and the pilot are considered a rigid body. Hence, we assume the pilot does not move or rotate with respect to the parafoil. The steering toggles are of course allowed to be pulled and released. However, this movement is translated into steering input, and does not affect the rigidity of the body.

3.2.1 Coordinate systems

In the formulation of the equations in the 6-DOF model we used the coordinate systems described below, also shown in Fig. 2.

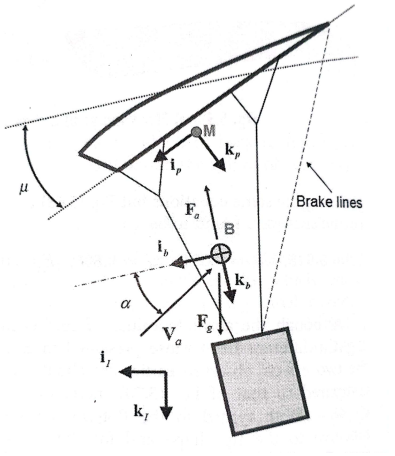

Fig. 2 6DOF parafoil-payload system [3]

NED inertial frame (in)

- Origin is fixed
- X positive in the true north direction (N)
- Y positive in the east direction (E)
- Z positive down (D)

Body frame (b)

- Origin in the center of gravity
- X_{body} is positive in the parafoil's longitudinal direction, in the parafoil's symmetry plane.
- Z_{body} is positive pointing down in the direction of the payload, in the parafoil's symmetry plane.
- Y_{body} is determined by the right hand rule

Wind frame (w)

- Origin in the center of gravity
- X_{wind} is positive in the direction of the velocity vector
- Z_{wind} is positive pointing down, in the parafoil's symmetry plane.
- Y_{wind} is determined by the right hand rule.

Parafoil fixed frame (p)

- Origin in the center of apparent mass (M)
- Same as body frame except for a rotation angle μ (rigging angle) around Y_{body}

3.2.2 Rotation matrices

To implement the 6-DOF model, we must first construct the rotation matrices that are used to transform between the coordinate systems mentioned above. The angles used for the construction of the rotation matrices are presented in Fig. 3.

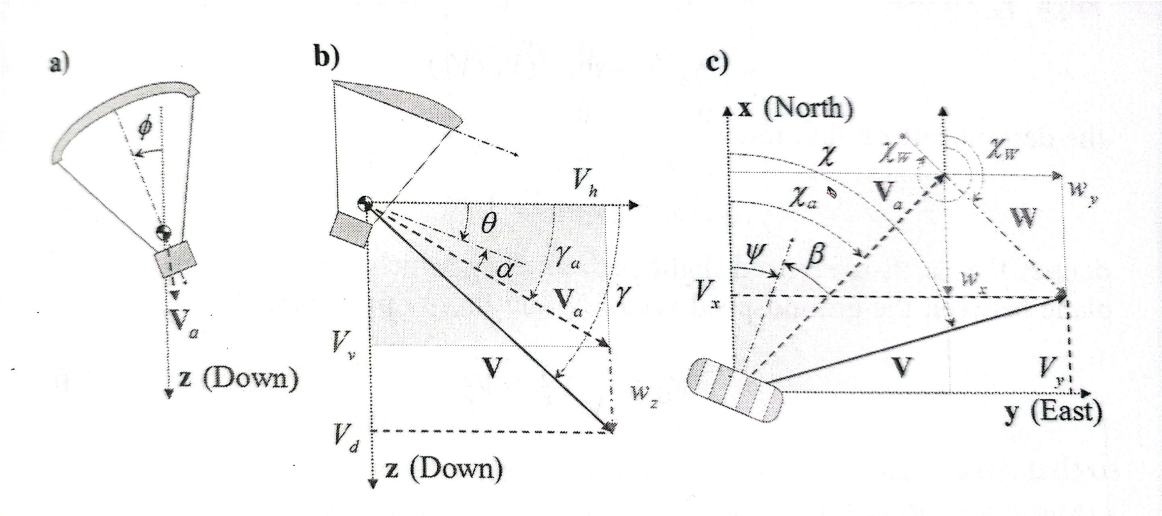

Fig. 3 parafoil-payload view from the front (a) side (b) and above (c) [3]

Wind to Body

The rotation matrix from wind frame to body frame is defined by the angle of attack α and the angle of bank β, as can be seen in Eq. (4) and in Eq. (5).

$$W \xrightarrow[3\ 2]{-\beta\ \alpha} B$$

$$R_\beta = \begin{bmatrix} cos(\beta) & sin(\beta) & 0 \\ -sin(\beta) & cos(\beta) & 0 \\ 0 & 0 & 1 \end{bmatrix} R_\alpha = \begin{bmatrix} cos(\alpha) & 0 & -sin(\alpha) \\ 0 & 1 & 0 \\ sin(\alpha) & 0 & cos(\alpha) \end{bmatrix} \tag{4}$$

$$R_W^b = R_\alpha R_\beta^T = \begin{bmatrix} cos(\alpha)cos(\beta) & -cos(\alpha)sin(\beta) & -sin(\alpha) \\ sin(\beta) & cos(\beta) & 0 \\ sin(\alpha)cos(\beta) & -sin(\alpha)sin(\beta) & cos(\alpha) \end{bmatrix} \tag{5}$$

Body to parafoil

The rotation matrix from body frame to parafoil frame is determined solely by a rotation around Y_p axis by the rigging angle μ, as can be seen in Eq. (6).

$$R_b^p = \begin{bmatrix} cos(\mu) & 0 & -sin(\mu) \\ 0 & 1 & 0 \\ sin(\mu) & 0 & cos(\mu) \end{bmatrix} \tag{6}$$

The angles α, β, μ are defined according to Fig 3.

NED to Body

The rotation matrix from the inertial frame to the body frame is defined by the 3 Euler angles ψ, θ, ϕ, in the following order $I \xrightarrow[3\ 2\ 1]{\psi\ \theta\ \phi} B$, and is calculated using Eq. (7) and Eq. (8).

$$R_\psi = \begin{bmatrix} cos(\psi) & sin(\psi) & 0 \\ -sin(\psi) & cos(\psi) & 0 \\ 0 & 0 & 1 \end{bmatrix} R_\theta = \begin{bmatrix} cos(\theta) & 0 & -sin(\theta) \\ 0 & 1 & 0 \\ sin(\theta) & 0 & cos(\theta) \end{bmatrix} R_\phi = \begin{bmatrix} 1 & 0 & 0 \\ 0 & cos(\phi) & sin(\phi) \\ 0 & -sin(\phi) & cos(\phi) \end{bmatrix} \tag{7}$$

$$R_{in}^b = R_\phi R_\theta R_\psi \tag{8}$$

Fig 3 shows how the Euler angles are defined.

3.2.3 External forces and moments

Gravity

The gravity force in body frame is expressed in Eq. (9).

$$F_g = mg \begin{bmatrix} -sin(\theta) \\ cos(\theta)sin(\phi) \\ cos(\theta)cos(\phi) \end{bmatrix} \tag{9}$$

Aerodynamic forces and moments

First, we must find the velocity of the body with respect to the wind. Since the velocity is known in body coordinates, it is simpler to express the relative velocity in the same system, using Eq. (10).

$$\bar{V}_a = \bar{V}_b - R_{in}^b \bar{W} \tag{10}$$

Where $V_a = \begin{bmatrix} V_{ax} \\ V_{ay} \\ V_{az} \end{bmatrix}$

The angle of attack α and the bank angle β can be derived from the components of V_a using Eq. (11) and Eq. (12).

$$\alpha = tan^{-1}\left(\frac{V_{az}}{V_{ax}}\right) \tag{11}$$

$$\beta = tan^{-1}\left(\frac{V_{ay}}{\sqrt{V_{ax}^2 + V_{ay}^2}}\right) \tag{12}$$

Now, it is possible to calculate the rotation matrix R_w^b using Eq. (4) and Eq. (5), and the aerodynamic forces using Eq. (13).

$$F_a = -\frac{1}{2}\rho V_a^2 S R_w^b \begin{bmatrix} C_{D0} + C_{D\alpha^2}\alpha^2 + C_{D\delta_s}\bar{\delta}_s \\ -C_{Y\beta}\beta \\ C_{L0} + C_{L\alpha}\alpha + C_{L\delta_s}\bar{\delta}_s \end{bmatrix} \tag{13}$$

Here, ρ is the density of the air, V_a is the airspeed defined at Eq. (10), S is the surface of the parafoil, b is the parafoil span, $C_{D0}, C_{D\alpha^2}, C_{D\delta_s}, C_{Y\beta}, C_{L0}, C_{L\alpha}$ are the stability derivatives, $\bar{\delta}_s$ is the normalized parafoil symmetric deflection input and $C_{L\delta_s}$ is the control derivative of $\bar{\delta}_s$. The x component of F_a is the drag force, and it is negative in body frame since it is opposite to the longitudinal direction of the body. The z component of F_a is the lift, and it is negative in body frame since z_b is positive down. However, The y component of F_a, i.e the side force, is positive in body frame since it increases with the increase in β.

The aerodynamic moments in body frame are given in Eq. (14).

$$M_a = \frac{1}{2}\rho V_a^2 S \begin{bmatrix} b(C_{l\beta}\beta + \frac{b}{2V_a}C_{lp}p + \frac{b}{2V_a}C_{lr}r + C_{l\delta_a}\bar{\delta}_a) \\ \bar{c}(C_{m0} + C_{m\alpha}\alpha + \frac{c}{2V_a}C_{mq}q) \\ b(C_{n\beta}\beta + \frac{b}{2V_a}C_{np}p + \frac{b}{2V_a}C_{nr}r + C_{n\delta_a}\bar{\delta}_a) \end{bmatrix} \tag{14}$$

Here, ρ, V_a, S, b are the same as in Eq. (13), $C_{lp}, C_{lr}, C_{mq}, C_{np}, C_{nr}, C_{l\beta}, C_{m0}, C_{m\alpha}, C_{n\beta}$ are the stability derivatives, $\bar{\delta}_a$ is the normalized parafoil asymmetric deflection input, and $C_{L\delta_a}$ is the control derivative of $\bar{\delta}_a$. $\bar{c}$ is the mean aerodynamic chord, in our model we assume the parafoil is a rectangle, hence $c = \bar{c}$. p, q, r are the components of the angular rate of the body in body coordinates, ω, as seen in 3.2.4.

Parafoil deflection input

The aerodynamic forces and moments depend on the symmetric and asymmetric deflections of the parafoil, δ_s, δ_a accordingly. Those deflections are determined by the left and right toggle inputs $\delta_{right}, \delta_{left}$ using Eq. (15). Note that $\bar{\delta}_a, \bar{\delta}_s$ in Eq. (16) are the deflection values normalized by the maximum deflection possible according to the parafoil properties.

$$\delta_a = \delta_{right} - \delta_{left} \qquad \delta_s = \delta_{right} + \delta_{left} \tag{15}$$

$$\bar{\delta}_a = \frac{\delta_a}{\delta_{smax}} \qquad \bar{\delta}_s = \frac{\delta_s}{\delta_{smax}} \tag{16}$$

3.2.4 Equations of motion

The equations of motion are a set of ordinary differential equations in the form of Eq. (17), where $\bar{V}$ contains linear and angular velocities, as shown in Eq. (18).

$$A\dot{\bar{V}} = B(\bar{V}^*) \tag{17}$$

$$\bar{V} = \begin{bmatrix} u & v & w & p & q & r \end{bmatrix}^T \tag{18}$$

The vector $\bar{V}_{body} = \begin{bmatrix} u & v & w \end{bmatrix}^T$ is the body velocity with respect to the inertial frame expressed in body coordinates.
The vector $\bar{\omega}_{body} = \begin{bmatrix} p & q & r \end{bmatrix}^T$ is the body angular rate with respect to the inertial frame expressed in body coordinates.

A_{6X6} is an invertible matrix that only contains parafoil properties and does not depend on the state. A_{6X6} is calculated using Eq. (19) and Eq. (20).

$$A = A_U + A_r A_L \tag{19}$$

$$\begin{aligned} A_U &= \begin{bmatrix} mI_{3x3} + I'_{a.m} & -I'_{a.m}s(r_{BM}) \\ 0_{3x3} & I + I'_{a.i} \end{bmatrix} A_r = \begin{bmatrix} I_{3x3} & 0_{3x3} \\ 0_{3x3} & s(r_{BM}) \end{bmatrix} A_L = \begin{bmatrix} 0_{3x3} & 0_{3x3} \\ I'_{a.m} & I'_{a.m}s(r_{BM}) \end{bmatrix} \\ A_\omega &= \begin{bmatrix} s(\omega) & 0_{3x3} \\ 0_{3x3} & s(\omega) \end{bmatrix} A_W = \begin{bmatrix} I'_{a.m}R^b_{in} & 0_{3x3} \\ 0_{3x3} & I'_{a.m}R^b_{in} \end{bmatrix} \end{aligned} \tag{20}$$

Here, m is the mass of both the payload, the parafoil and the air entrapped in it and r_{BM} is the vector from the center of mass to the center of apparent mass in body coordinates. $I'_{a.m}$ and $I_{a.i}$ are the matrices of apparent mass and apparent inertia, respectively, as defined in Eq. (22) based on subsection 3.1 . I_{3x3} is the identity matrix, and 0_{3x3} is a matrix containing only zeros. The notion $s(x)$ denote a skew symmetric matrix derived from the vector x.

B_{6X1} is a vector that depends on $\bar{V}$, on external forces and moments F_a, F_g, M_a, and on wind conditions $\bar{W}$. B_{6X1} is calculated using Eq. (21).

$$\bar{B} = \begin{bmatrix} F_a + F_g \\ M_a \end{bmatrix} - [A_\omega A_U + A_r A_\omega A_L]\bar{V}^* + A_r A_\omega A_W \begin{bmatrix} \bar{W} \\ \bar{W} \end{bmatrix} \tag{21}$$

Note, that the relations in Eq. (22) were used to reduce the size of the matrix.

$$I'_{a.m} = R^b_p I_{a.m} R^p_b \qquad I'_{a.i} = R^b_p I_{a.i} R^p_b \tag{22}$$

Rotational kinematics is used in Eq. (23) to find $\begin{bmatrix} \dot{\phi} & \dot{\theta} & \dot{\psi} \end{bmatrix}^T$ which are the rates of the Euler angles between body and inertial systems.

$$\begin{bmatrix} \dot{\phi} \\ \dot{\theta} \\ \dot{\psi} \end{bmatrix} = \begin{bmatrix} 1 & sin(\phi)tan(\theta) & cos(\phi)tan(\theta) \\ 0 & cos(\phi) & -sin(\phi) \\ 0 & \frac{sin(\phi)}{cos(\theta)} & \frac{cos(\phi)}{cos(\theta)} \end{bmatrix} \begin{bmatrix} p \\ q \\ r \end{bmatrix} \tag{23}$$

Translation kinematics is used in Eq. (24) to calculate the position of the body in the inertial system $\begin{bmatrix} x_{in} & y_{in} & z_{in} \end{bmatrix}^T$.

$$\begin{bmatrix} \dot{x}_{in} \\ \dot{y}_{in} \\ \dot{z}_{in} \end{bmatrix} = R_b^{in} V_{body} \tag{24}$$

Finally, the full state vector is presented in Eq. (25), and can be solved using the differential equation mentioned above and a set of initial conditions.

$$\bar{X}_{12X1} = \begin{bmatrix} u & v & w & p & q & r & \phi & \theta & \psi & x_{in} & y_{in} & z_{in} \end{bmatrix}^T \tag{25}$$

3.3 9-DOF Model

In addition to the 6-DOF model we chose to develop a high fidelity 9-DOF model for the parafoil-pilot system. In this model the parafoil and the pilot are not considered a rigid body since we allow the pilot to rotate with respect to the parafoil. The nine degrees of freedom are translations along 3 axes and rotations around 3 axes for the parafoil, and rotations around 3 axes for the pilot. We divide the system into two parts: subsystem 1, which is the parafoil, and subsystem 2, which is the payload (in our case, pilot).

Since there is no translation between the parafoil and the payload, the entire system can be described by a single velocity, V_c, acting on the connection point between parafoil and payload (point 'c' in Fig. 4).

3.3.1 Coordinate systems

In the formulation of the equations in the 9-DOF model we used similar coordinate systems as in the 6-DOF model, with some changes and additions. These coordinate system are shown in Fig. 4.

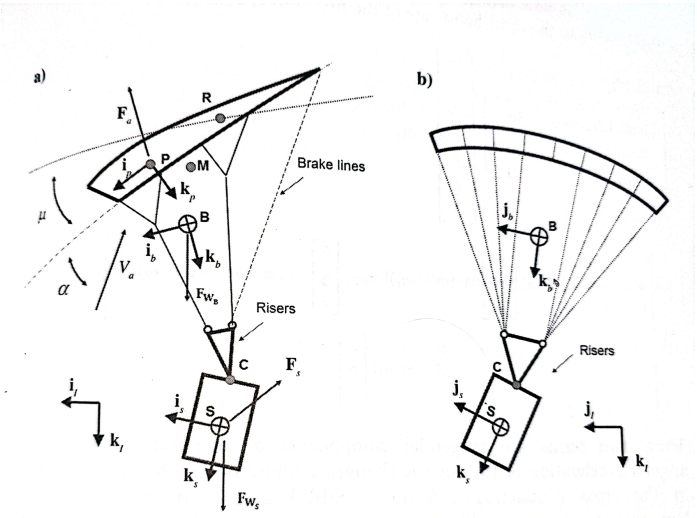

Fig. 4 9-DOF parafoil-payload system [3]

NED frame (in) - same as in 6-DOF.

Body frame (b) - same as in 6-DOF except the origin is at the center of mass of subsystem 1, the parafoil.

Wind frame (w) - same as in 6-DOF except the origin is at the center of mass of subsystem 1, the parafoil.

Parafoil fixed frame (p) - same as in 6-DOF except the origin is at the aerodynamic center of of subsystem 1, the parafoil.

Payload frame (s)

- Origin in the center of gravity of the payload (pilot)
- X_s is positive in the payload's longitudinal direction, in the payload's symmetry plane.
- Z_s is positive pointing down in the opposite direction of the parafoil, in the payload's symmetry plane.
- Y_s is determined by the right hand rule

Reference points

The following reference points were defined:

- C - connection point between subsystem 1 (parafoil) and subsystem 2 (payload). It is the point where the risers of the parafoil attach to the payload. Since the payload is free to rotate with respect to the parafoil, we define that the moments applied by this point are zero $\bar{M}_c = \bar{0}$. The connection point does apply an internal force $\bar{F}_c$ on both systems.
- P - parafoil's aerodynamic center
- R - parafoil rotation point
- M - center of apparent mass
- B - parafoil center of mass (*)
- S - Payload center of mass (s)

3.3.2 Rotation matrices

The rotation matrices used in the 6-DOF model, R_b^p, R_{in}^b are valid, With the addition of 2 matrices.

Body to payload

R_b^s is the rotation matrix from body frame to payload frame. It is calculated by substituting the Euler angles ϕ_s, θ_s, ψ_s, that represent the attitude of the payload relative to the body, to Eq. (8). The order of rotation is similar to that used in the 6-DOF model:

$$B \xrightarrow[3\ \ 2\ \ 1]{\psi_s\ \ \theta_s\ \ \phi_s} S$$

Wind to parafoil

The rotation matrix from wind frame to parafoil frame is calculated using Eq. (4) and Eq. (5) from the 6-DOF model. However, in the 9-DOF the angles α, β are obtained using the airspeed of the aerodynamic center, that is calculated in Eq. (28). The order of rotation is similar to that used in the 6-DOF model:

$$W \xrightarrow[3\ 2]{-\beta\ \alpha} P$$

3.3.3 External forces and moments

The external forces and moments are calculated separately for the parafoil and payload. For the parafoil they are denoted with asterisks x^*, and for the payload with x^s.

Gravity

The gravity force acting on the parafoil, F_g^*, is the same as in the 6-DOF model. The gravity force acting on the payload is expressed in Eq. (26).

$$F_g^s = m_s g R_b^s \begin{bmatrix} -sin(\theta) \\ cos(\theta)sin(\phi) \\ cos(\theta)cos(\phi) \end{bmatrix} \tag{26}$$

Aerodynamic forces and moments

The aerodynamic center is the point where the aerodynamic moments do not depend on the angle of attack, $C_{m\alpha} = 0$. Therefore, it is beneficial to calculate the aerodynamic moments around the aerodynamic center. For that reason, we chose to express the forces in the parafoil frame, where the origin coincides with the aerodynamic center.

The velocity of the aerodynamic center in reference to the inertial frame and expressed in parafoil coordinates, is given in Eq. (27).

$$V_p = R_b^p (V_c + s(\omega) r_{CP}) \tag{27}$$

The velocity of the aerodynamic center in reference to the wind frame, expressed in parafoil coordinates, is given in Eq. (28).

$$V_{pa} = V_p - R_{in}^p W \tag{28}$$

The angle of attack α and the bank angle β can be derived from the components of V_{pa} using Eq. (11) and Eq. (12), similarly to the 6-DOF model. Using α, β it is possible to calculate the rotation matrix R_w^p using Eq. (5).

Finally, the aerodynamic forces acting on the parafoil subsystem, expressed in body coordinates, are shown in Eq. (29).

$$F_a^* = -\frac{1}{2}\rho V_{pa}^2 S_p R_p^b R_w^p \begin{bmatrix} C_{D0} + C_{D\alpha^2}\alpha^2 + C_{D\delta_s}\bar{\delta_s} \\ -C_{Y\beta}\beta \\ C_{L0} + C_{L\alpha}\alpha + C_{L\delta_s}\bar{\delta_s} \end{bmatrix} \tag{29}$$

And the aerodynamic moments acting on the parafoil subsystem, expressed in body coordinates, are shown in Eq. (30).

$$M_a^* = \frac{1}{2}\rho V_{pa}^2 S_p R_p^b \begin{bmatrix} b(C_{l\beta}\beta + \frac{b}{2V_a}C_{lp}\tilde{p} + \frac{b}{2V_a}C_{lr}\tilde{r} + C_{l\delta_a}\bar{\delta_a}) \\ \bar{c}(C_{m0} + \frac{c}{2V_a}C_{mq}\tilde{q}) \\ b(C_{n\beta}\beta + \frac{b}{2V_a}C_{np}\tilde{p} + \frac{b}{2V_a}C_{nr}\tilde{r} + C_{n\delta_a}\bar{\delta_a}) \end{bmatrix} \tag{30}$$

Note, that $\tilde{p}, \tilde{q}, \tilde{r}$ are the parafoil angular rates expressed in the parafoil frame (p).

For the payload subsystem, we assume that the all the aerodynamic forces are drag forces, since the payload does not generate lift. In addition, we assume $M_a^s \approx 0$.

The velocity of the payload center of mass in reference to the inertial frame and expressed in payload coordinates, is given in Eq. (31).

$$V_s = R_b^s(V_c + s(\omega_s)r_{CS}) \tag{31}$$

Similarly, the velocity of the payload center of mass in reference to the wind frame, expressed in payload coordinates, is given in Eq. (32).

$$V_{sa} = V_s - R_{in}^s W \tag{32}$$

Finally, the aerodynamic forces acting on the payload subsystem expressed in payload coordinates are shown in Eq. (33).

$$F_a^s = -\frac{1}{2}\rho C_D^s V_{sa}^2 \hat{V}_{sa} \tag{33}$$

3.3.4 Equations of motion

Similar to the 6-DOF model, the equations of motion of the 9-DOF model are a set of ordinary differential equations in the form of Eq. (17), where the state vector $\bar{V}_{12x1}$ is given in Eq. (34).

$$\bar{V} = \begin{bmatrix} u_c & v_c & w_c & p & q & r & p_s & q_s & r_s & F_{cx} & F_{cy} & F_{cz} \end{bmatrix}^T \tag{34}$$

$\bar{V}_c = \begin{bmatrix} u_c & v_c & w_c \end{bmatrix}^T$ is the connection point velocity with respect to the inertial frame, expressed in body coordinates.

$\bar{\omega}_{body} = \begin{bmatrix} p & q & r \end{bmatrix}^T$ is the parafoil angular rate with respect to the inertial frame expressed in body coordinates.

$\bar{\omega}_s = \begin{bmatrix} p_s & q_s & r_s \end{bmatrix}^T$ is the payload angular rate with respect to the inertial frame expressed in payload coordinates.

$\bar{F}_c = \begin{bmatrix} F_{cx} & F_{cy} & F_{cz} \end{bmatrix}^T$ are the forces acting at the connection point expressed in body coordinates. We chose to add the three component of F_c to the state vector since they are unknown and it is simpler to calculate them numerically at each step than to eliminate them algebraically.

A_{12X12} is an invertible matrix that only contains parafoil properties and does not depend on the state, as can be seen in Eq. (35).

$$A_{12X12} = \begin{bmatrix} m^* I_{3x3} + I'_{a.m} & -I'_{a.m} s(r_{CM}) - m^* s(r_{CB}) & 0_{3x3} & -I_{3x3} \\ s(r_{BM}) I'_{a.m} & I^* + I'_{a.i} - s(r_{BM}) I'_{a.m} s(r_{CM}) & 0_{3X3} & S(r_{CB}) \\ m_s R^s_b & 0_{3x3} & -m_s s(r^s_{CS}) & R^s_b \\ 0_{3x3} & 0_{3x3} & I_s & -s(r^s_{CS}) R^s_b \end{bmatrix} \tag{35}$$

B_{12X1} is a vector that depends on $\bar{V}$, on external forces and moments $F^*_a, F^*_g, M^*_a, F^s_a F^s_g, M^s_a$, and on wind conditions $\bar{W}$. It is calculated using equations Eq. (36) and Eq. (37).

$$\begin{aligned} B1 &= F^*_a + F^*_g - s(\omega)[(m^* I_{3x3} + I'_{a.m}]\bar{V}_c + s(\omega) I'_{a.m} s(r_{CM})\bar{\omega} - m^* s(\omega) s(\omega) r_{CB} + s(\omega) I'_{a.m} R^b_{in} W \\ B2 &= M^*_a + s(r_{BP}) F^*_a - [s(\omega)(I^* + I'_{a.i}) - s(r_{BM}) s(\omega) \\ &\quad I'_{a.m} s(r_{CM})]\bar{\omega} - s(r_{BM}) s(\omega) I'_{a.m} \bar{V}_c \; + s(r_{BM}) s(\omega) I'_{a.m} R^b_{in} W \\ B3 &= F^s_a + F^s_g - m_s R^s_b s(\omega) \bar{V}_c - m_s s(\omega^s_s) s(\omega^s_s) r^s_{CS} \\ B4 &= M^s_a - s(\omega^s_s) I_s \bar{\omega}_s \end{aligned} \tag{36}$$

$$\bar{B} = \begin{bmatrix} B1 \\ B2 \\ B3 \\ B3 \end{bmatrix} \tag{37}$$

Rotational kinematics is used to find $\begin{bmatrix} \dot{\phi} & \dot{\theta} & \dot{\psi} \end{bmatrix}^T$, which are the rates of the Euler angles between body and inertial systems, using Eq. (23) from the 6-DOF model. Similarly, $[\dot{\phi}_s,\ \dot{\theta}_S,\ \dot{\psi}_s]^T$ are calculated using the same equation,

substituting the payload angular rates ω_s.

Translation kinematics is used to calculate the position of the body in the inertial frame. This is similar to what was done in the 6-DOF model, except that the connection point velocity V_c is used, as can be seen in Eq. (38).

$$\begin{bmatrix} \dot{x}_{in} \\ \dot{y}_{in} \\ \dot{z}_{in} \end{bmatrix} = R_b^{in} V_c \tag{38}$$

Finally, the full state vector is presented in Eq. (39), and can be obtained by solving the differential equation mentioned above with a set of initial conditions.

$$\bar{X} = \begin{bmatrix} u_c & v_c & w_c & p & q & r & \phi & \theta & \psi & x_{in} & y_{in} & z_{in} & p_s & q_s & r_s & F_{cx} & F_{cy} & F_{cz} & \phi_s & \theta_s & \psi_s \end{bmatrix}^T \tag{39}$$

3.4 Atmospheric model

The aerodynamic forces and moments depend on the density of the air, which in turn depends on the flight altitude. In parafoil flight, it is given that the altitude decreases constantly during the flight, and so, the density changes continuously. To account for this change, a simple atmospheric model was implemented in the simulation. The model receives the altitude of the flight as an input from the simulation, where $h = -Z_{in}$. The chosen model assumes standard atmosphere and linear change in temperature in the troposphere, which is the lowest layer of Earth's atmosphere, where the parafoil flight takes place. The formula for the density is shown in Eq. (40) [11].

$$\rho = \rho_0 \left(1 - \frac{Lh}{T_0}\right)^{\frac{g_0}{L*R}-1} \tag{40}$$

where $\rho_0 = 1.225\ [\frac{kg}{m^3}]$, $L = -0.0065\ [\frac{K}{m}]$, $T_0 = 15\ [^oC]$, $g_0 = 9.81\ [\frac{m}{s^2}]$, $R = 287\ [\frac{J}{kgK}]$

4 Simulator

4.1 Simulator architecture

The simulator is a real time system that receives steering inputs from the user and continuously presents the position and orientation of the canopy. The simulator consists of two main components: the backbone and the real-time interface. The backbone is an ode45 Matlab solver that propagates the differential equations of motion presented in the dynamic 6-DOF model in section 3 over a short time ($< 1[s]$). The real-time interface is a timer Matlab function that receives user key inputs, samples the backbone a few times a second, and presents the graphic data to the user. The simulator

also stores the flight data, and it can be viewed once the real-time simulation stops. Fig. 5 presents a flow chart of the simulator.

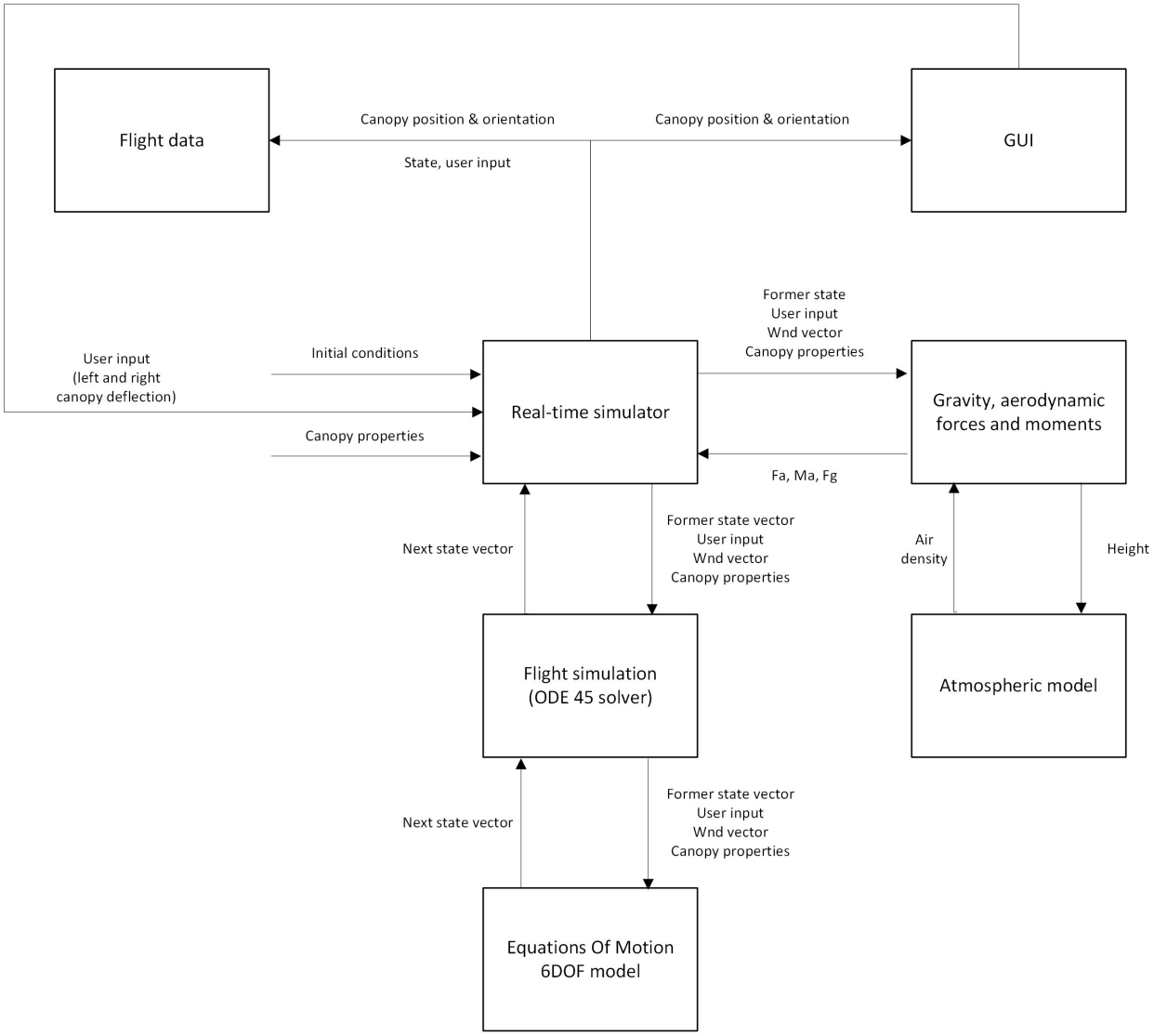

Fig. 5 Simulator flow chart

4.2 Graphic User Interface

The graphic user interface consists of a single figure that shows the flight of the canopy in the "natural" environment. The figure updates continuously a few times a second to give the user a sense of a smooth flight. To simply model the canopy we used a rectangle with colored edges as can be seen in Fig. 6. The green and pink lines correspond to the directions of X_{body} and Y_{body} respectively, and are designed to provide the user with a sense of the canopy's orientation. The red line that drags on from the canopy shows the last part of the flight path, and is designed to provide the user with a sense of the canopy's current position in reference to its former position. The "natural" environment of the simulator

includes spherical "bubbles" that symbol the air, and a brown sheet that symbols the ground. The bubbles are spread randomly in space, and their sole purpose is to provide a sense of direction to the user. Fig. 7 provides a bird's eye view of the simulator environment. Note, that the "natural" environment is bounded to a few hundred meters at each direction, to prevent high consumption computational resources that can potentially slow the simulation. At the end of the simulation, the user is presented with the collected flight data, as can be seen in section 5.

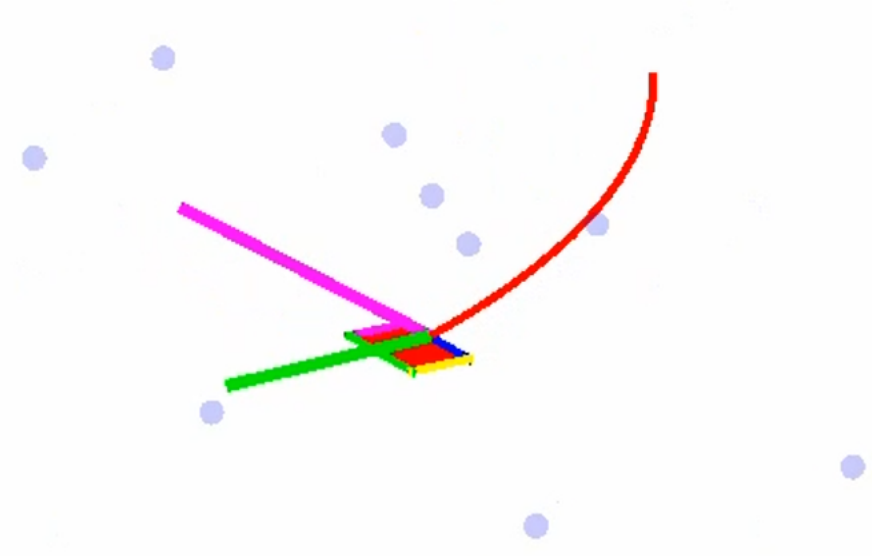

Fig. 6 User's view of the simulator

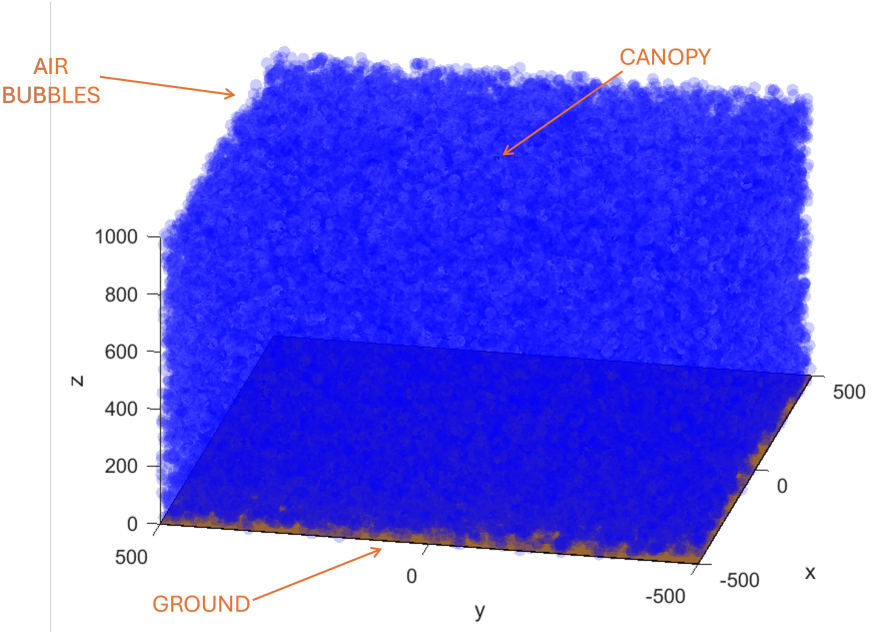

Fig. 7 Bird's eye view of the simulator

5 Results

Both the 6-DOF and 9-DOF simulations were tested to ensure that the models was implemented correctly and that the canopy behaves as expected. This chapter provides an in-depth explanation of the results.

5.1 6-DOF simulation results

Initial conditions

The initial conditions correspond to a payload being dropped from an airplane, with a parachute deploying moments afterward. This scenario results in both forward and downward velocity components, and an initial altitude of 1 $[km]$. For simplicity, we chose the forward velocity to be in the north direction, which coincides with X_{body} at the first moment of the flight. Therefore, in the NED inertial frame the initial conditions are:

$$V_{NED}(t=0) = \begin{bmatrix} 6.5 \\ 0 \\ 3.5 \end{bmatrix} [\frac{m}{s}], \qquad Position(t=0) = \begin{bmatrix} 0 \\ 0 \\ -1000 \end{bmatrix} [m]$$

In addition, we chose to account for potential deviation during deployment, by selecting an initial roll angle: $\phi_0 = 15[deg]$. The initial angular rates as well as the wind components were set to zero. By expressing the initial velocity in the body frame using the chosen initial Euler angles, we obtain the initial state vector, which is consistent with Eq. (25).

$$\bar{X}_{12X1} = \begin{bmatrix} 6.5[\frac{m}{s}] & 0.91[\frac{m}{s}] & 3.38[\frac{m}{s}] & 0 & 0 & 0 & 0.262[rad] & 0 & 0 & 0 & 0 & -1000[m] \end{bmatrix}^T$$

Flight path

Fig. 8 shows the flight path of the canopy. The canopy begins the flight at the blue asterisk, travels north, and then turns right. The canopy spirals down for two full circles, continues north, and then turns left. After a short spiraling, the canopy continues to travel southeast until the simulation stops.

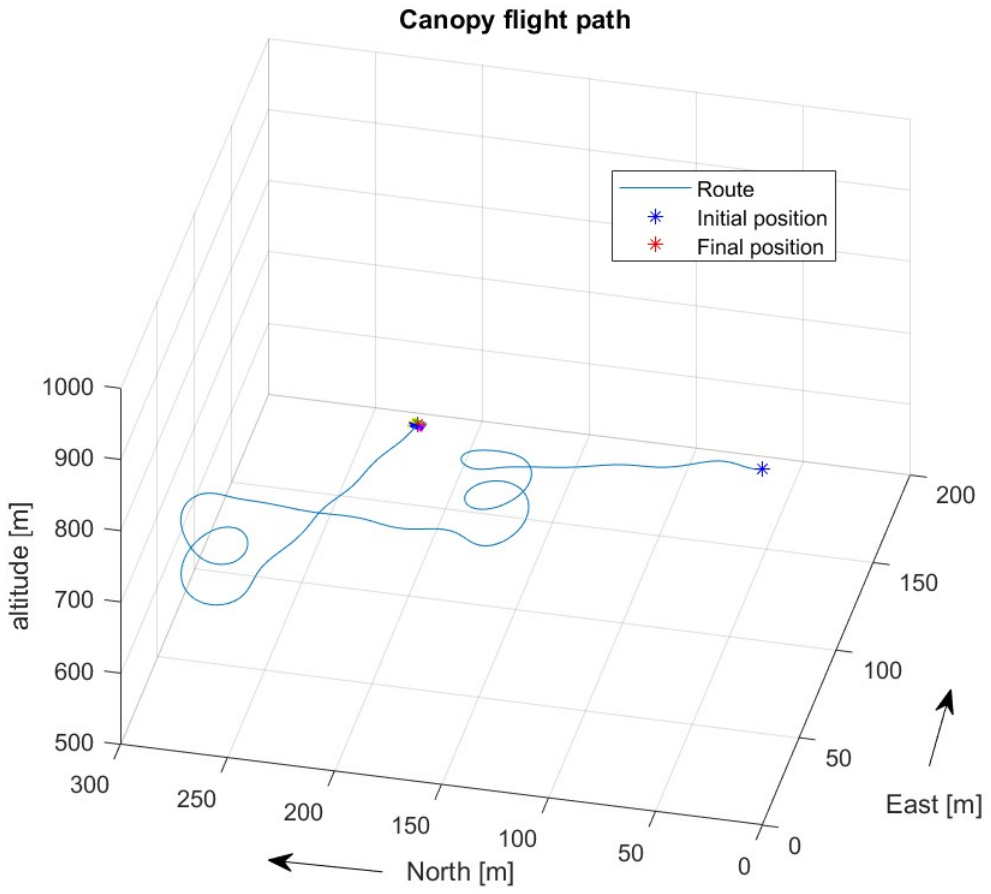

Fig. 8 Flight path

Steering input

Fig. 9 shows the steering input during the flight. The steering input is calculated based on the user's keystrokes using Eq. (15) and Eq. (16), presented below for convenience:

$$\delta_a = \delta_{right} - \delta_{left} \qquad \delta_s = \delta_{right} + \delta_{left}$$

$$\bar{\delta}_a = \frac{\delta_a}{\delta_{s\,max}} \qquad \bar{\delta}_s = \frac{\delta_s}{\delta_{s\,max}}$$

As expected, the right turn of the canopy (15 [s] to 50 [s]) is a result of right side canopy deflection, meaning $\delta_a = \delta_s > 0$. The left turn of the canopy (70 [s] to 100 [s]) is a result of left side canopy deflection, meaning $\delta_a = -\delta_s$. The canopy flare at the final part of the flight (105 [s] to end) is a result of symmetric canopy deflection, meaning, $\delta_a = 0, \delta_s > 0$.

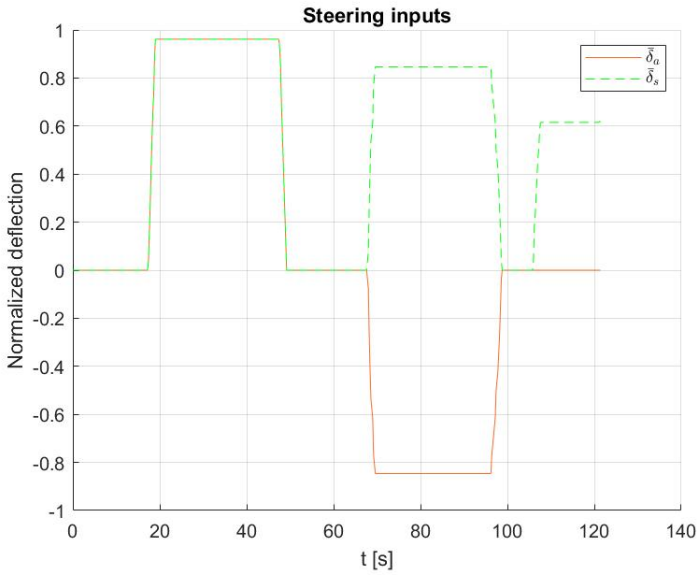

Fig. 9 Steering input

Angular rates

Fig. 10 shows the canopy angular rates during the flight. It is visible that the angular rates correspond to the steering input and flight path. The yaw rate *r* (represented by the black line) is positive when the canopy turns right, negative when it turns left, and perturbs around zero when the canopy flies straight. Moreover, the yaw rate is approximately constant during constant asymmetric steering input.

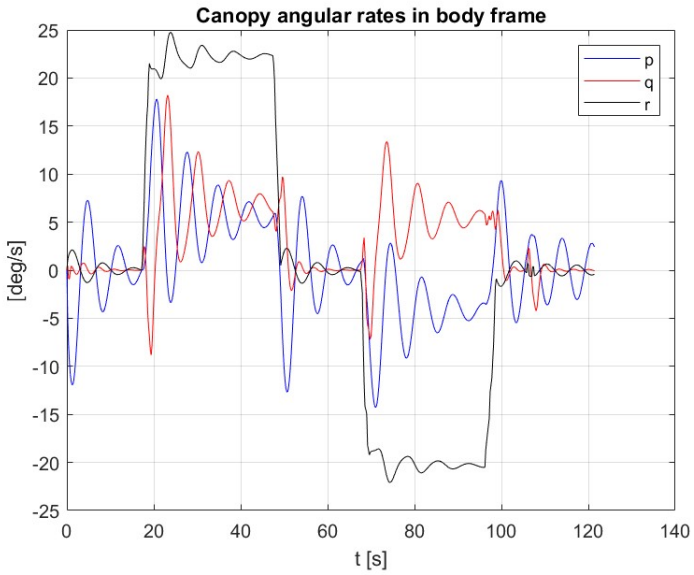

Fig. 10 Angular rates

Euler angles

Fig. 11 shows the attitude of the canopy during the flight, represented by Euler angles. The yaw angle ψ (represented by the black line) behaves as expected. At the beginning of the flight, the canopy is heading north, hence, $\psi = 0$. During the right turn of the canopy, ψ increases at a constant rate, while the canopy completes two spirals, until it settles at a constant value when the canopy continues straight. Similarly, during the left turn of the canopy, ψ decreases at a constant rate, while the canopy completes almost two spirals. At the final part of the flight, when the canopy flies straight in the southeast direction, ψ settles at a constant, non-zero, value, as expected.

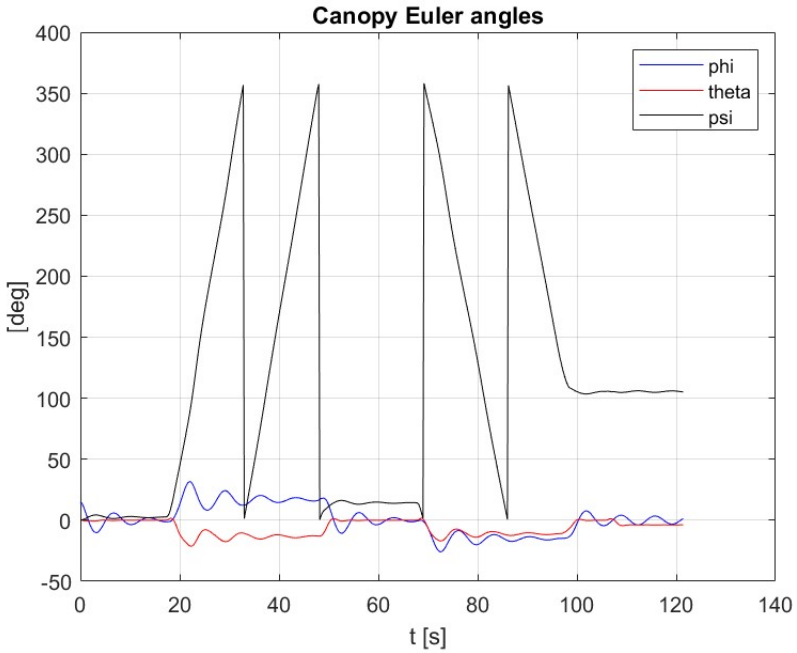

Fig. 11 Euler angles

Fig. 12 shows a close-up of the pitch and roll angles. The initial roll angle was $\phi(0) = 15\ [deg]$. As seen in the graph, within the first 15 seconds of the flight, ϕ (represented by the blue line) converges and remains bounded at a small value of 2 $[deg]$. Given more time to stabilize, it is likely that ϕ would have converged to zero. ϕ is positive when the canopy turns right and negative when it turns left. This is expected since asymmetric steering creates a corresponding aerodynamic moment around Y_{body}, as seen in Eq. (14). The moment tilts the canopy, creating a positive or a negative roll angle, according to the direction of the turn.

The pitch angle θ (represented by the red line) is negative when the canopy turns, as the leading edge is pointed slightly downwards. Contrary to expectations, the pitch angle θ is negative at the end of the flight. For large skydiving canopies, a symmetric deflection is expected to cause the canopy to flare, resulting in a significant and long increase in the pitch angle. However, for small canopies, such as the "SnowFlake" used in our model, the small increase in pitch angle (at 105 [s]) can be enough to stall the canopy. Immediately after the stall, the canopy will pitch down until it stabilizes,

provided the altitude allows enough time for recovery. Hence, the unexpected behaviour does not necessarily indicates an error in the implementation of the model.

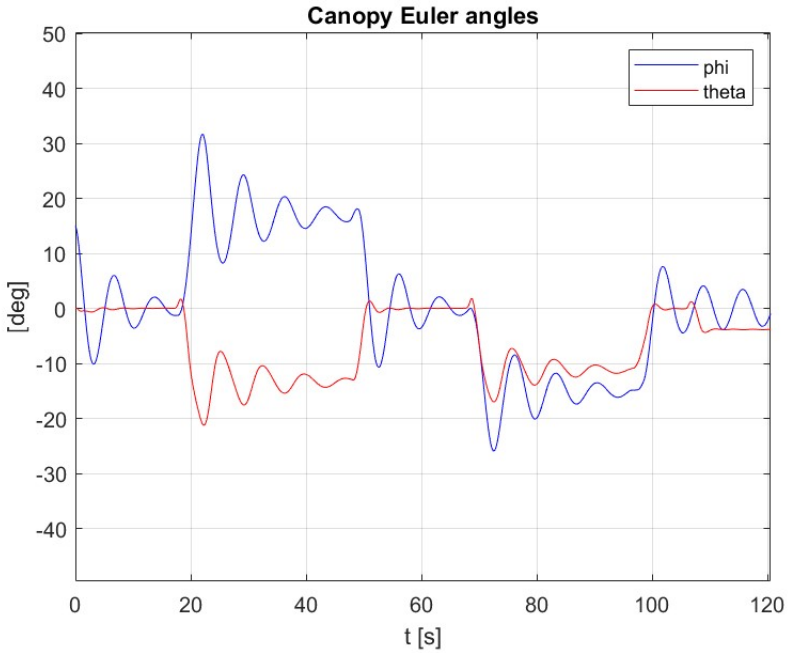

Fig. 12 Euler angles close-up

Canopy velocity

Fig. 13 shows the canopy velocity during the flight in body coordinates. The velocity v in the direction of Y_{body} (represented by the red line) is negative during a right turn and positive during a left turn. This indicates that the turns are not coordinated, causing the pilot to experience a side force due to inertia. In order to initiate a coordinated turn, a canopy pilot needs to lean into the turn (by the means of his harness). therefore, reconstructing coordinated turns in simulation requires the 9-DOF model, which allows the roll angle between the payload and the parafoil. It can also be observed that v is negative for a right turn, indicating a negative bank angle, and positive for a left turn, indicating a positive bank angle.

The velocity in the direction of X_{body}, u, (represented by the blue line) and the velocity in the direction of Z_{body}, w, (represented by the black line) behave in a similar manner during the flight. When the canopy starts turning, u and w decrease and remain constant for the duration of the turn. At the end of the flight, u and w also decrease due to the symmetric deflection input (the flare of the canopy). The decrease in u and w is a result of the deflection of the canopy, which increases the angle of attack, thus increasing drag and lift and reducing u and w.

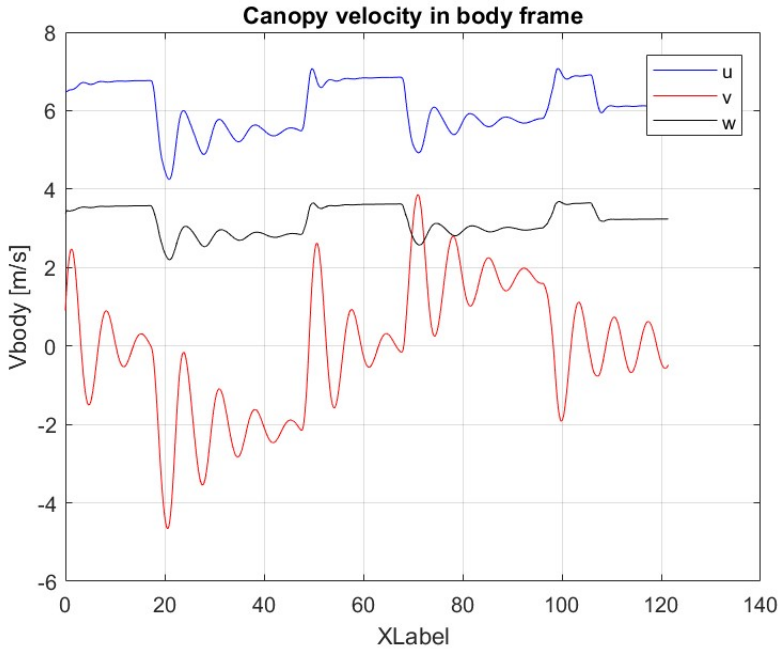

Fig. 13 Velocity in body frame

Fig. 14 shows the velocity in NED inertial coordinates. As expected, we see oscillations in V_{north} and V_{east} when the canopy spirals left and right, and they remain bounded when the canopy flies straight.

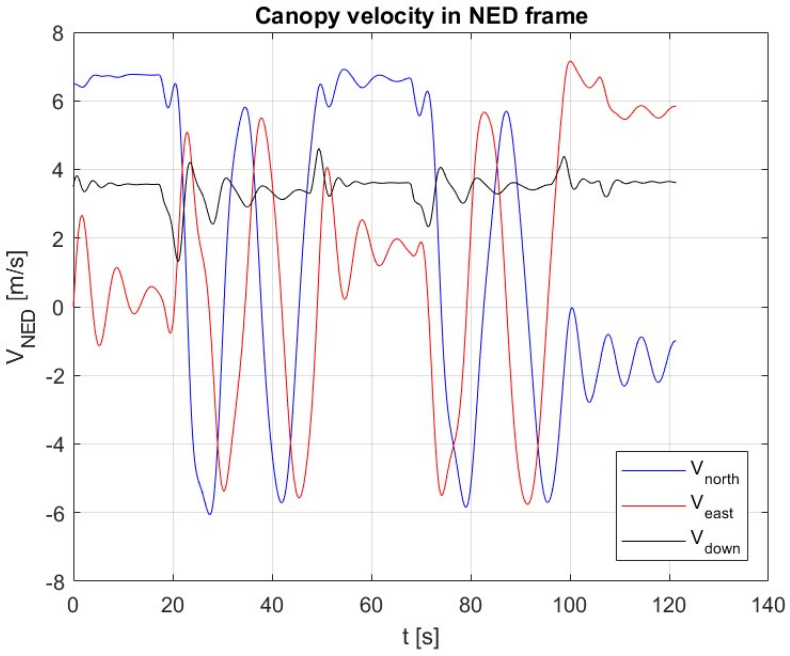

Fig. 14 Velocity in NED frame

5.2 9-DOF simulation results

Initial conditions

The initial position and velocity in the NED inertial frame:

$$V_{NED}(t=0) = \begin{bmatrix} 5 \\ 0 \\ 5 \end{bmatrix} [\frac{m}{s}], \quad Position(t=0) = \begin{bmatrix} 0 \\ 0 \\ -1000 \end{bmatrix} [m]$$

Therefore, the initial state vector, which is consistent with Eq. (39).

$$\bar{X}_{21X1} = \begin{bmatrix} 5 & 0 & 5 & 0 & 0 & 0 & 0 & 0 & \psi & 0 & 0 & -1000 & 0 & 0 & 0 & 0 & 0 & 0 & 0 & 0 & 0 \end{bmatrix}^T$$

Flight path

Fig. 15 shows the flight path of the canopy. The canopy begins the flight at the blue asterisk, travels north, and then turns right. The canopy spirals down for almost two circles, continues north-west, and then turns left. After spiraling down, the canopy continues to travel north until the simulation stops.

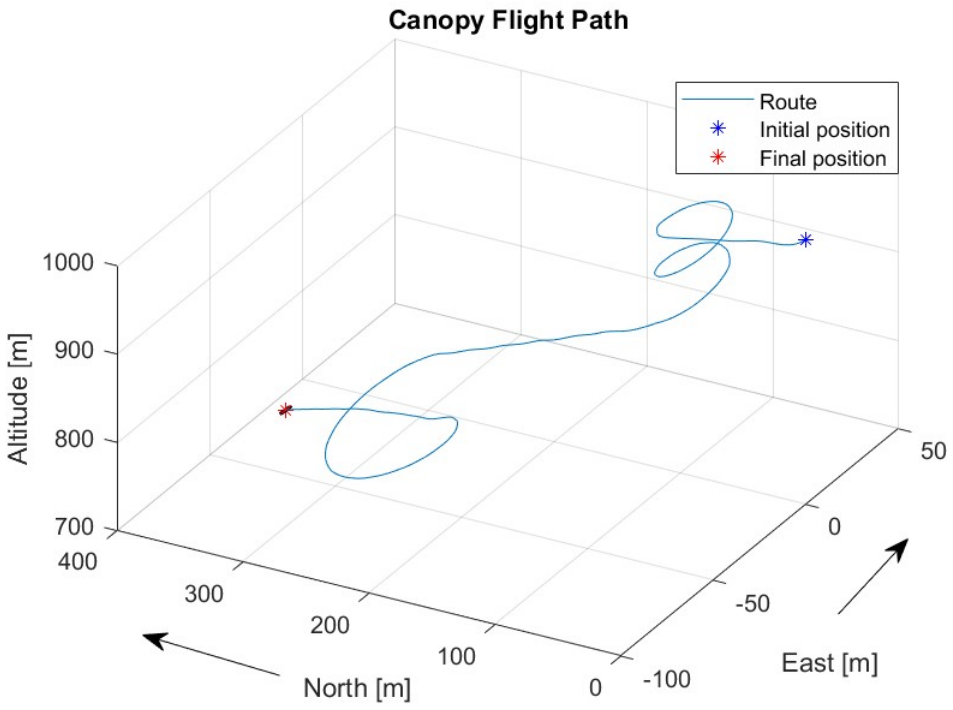

Fig. 15 Flight path

Steering input

Fig. 16 shows the steering input during the flight. we can see that the steering inputs correspond with the canopy turns.

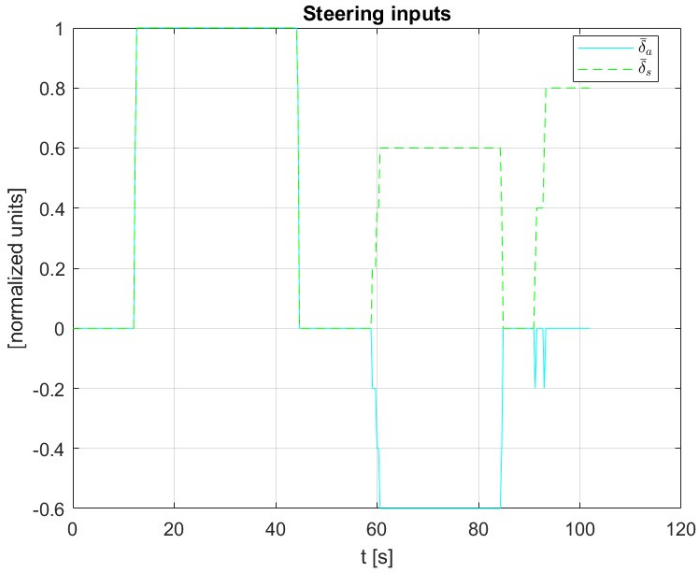

Fig. 16 Steering input

Angular rates

Figure 17 shows the angular rates of the canopy during flight, demonstrating a clear correlation with its flight path. Nevertheless, the angular rates show significantly more perturbations compared to the 6-DOF simulation. This variation is especially noticeable in the roll rate p. The perturbations can even be seen by the user during the real-time simulation.

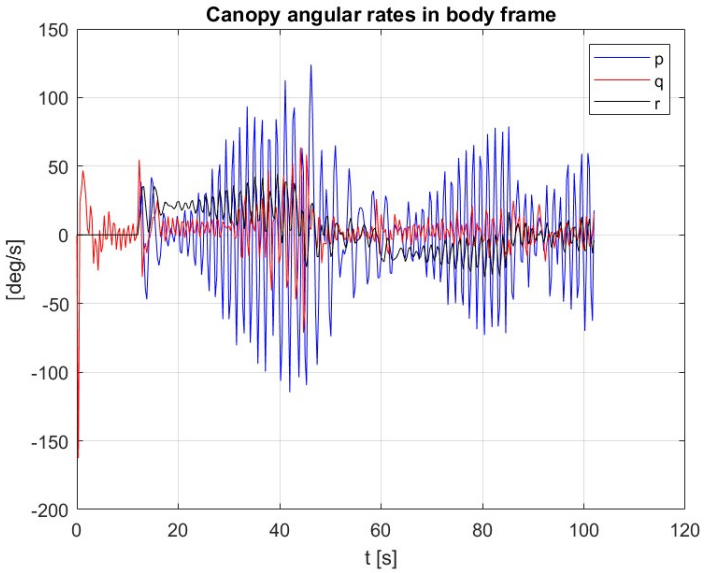

Fig. 17 Angular rates

Euler angles

Fig. 18 shows the attitude of the canopy during the flight, represented by Euler angles. Once again, the results align with the canopy's flight path. Additionally, there is significantly more perturbation compared to the 6-DOF model. This is particularly visible in the roll angle ϕ, which corresponds to the substantial perturbations in p discussed earlier.

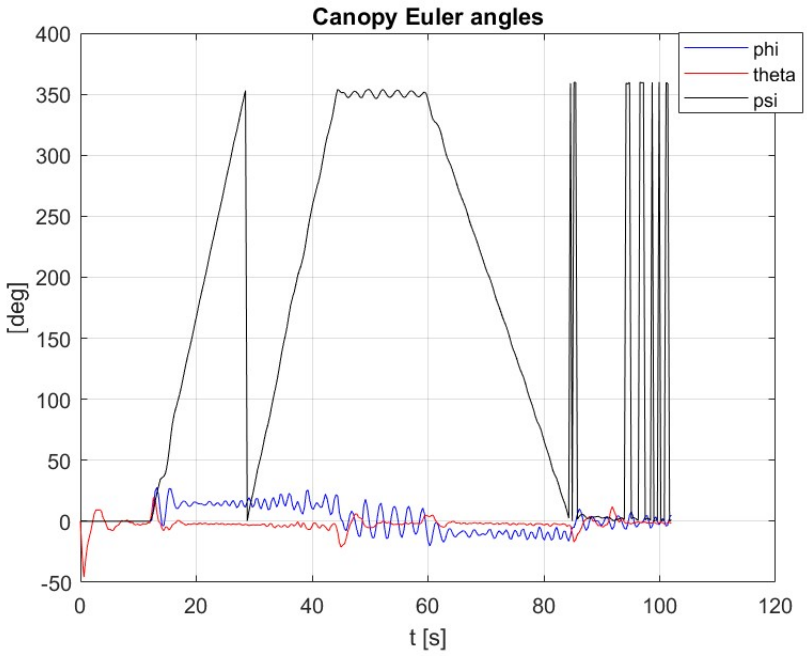

Fig. 18 Euler angles

Canopy velocity

Fig. 19 shows the canopy velocity during the flight in body coordinates. The velocity v in the direction of Y_{body} (represented by the red line) perturbs around zero during turns. Hence, the bank angle also perturbs around zero as well. This indicates that the pilot experiences osculating side forces due to inertia. As mentioned in the 6-DOF chapter, in order to initiate a coordinated turn a pilot needs to use his harness to lean into the turn. This maneuver causes a roll angle between the payload and the canopy, that is not allowed in the 6-DOF model, but is allowed on the 9-DOF model. Therefore, we see that the turns in the 9-DOF model are in fact coordinated on average. Note that the jumps in yaw angle at the end of the flight are due to bounding of the yaw angle between 0 and 360$[deg]$. In fact, psi perturbs around zero.

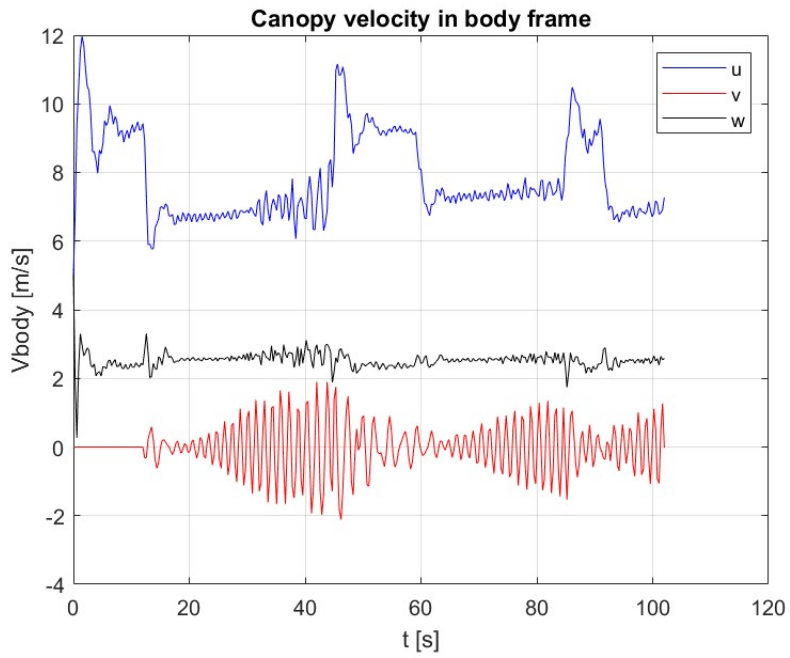

Fig. 19 Velocity in body frame

Fig. 20 shows the velocity in NED inertial coordinates. As expected, we see large oscillations in V_{north} and V_{east}, with an addition of small high frequency perturbations that are not seen in the 6-DOF model.

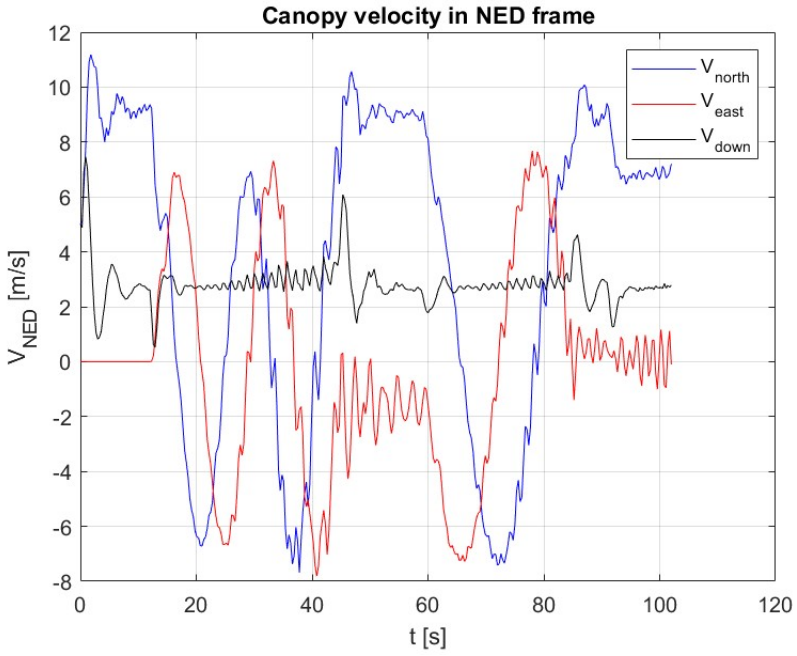

Fig. 20 Velocity in NED frame

Payload relative attitude

Fig. 21 shows the relative attitude of the payload (pilot) in reference to the canopy, represented by Euler angles. During the sharp right turn the payload begins to rotates in reference to the canopy, as seen by the relative yaw angle ψ_s. This is most likely due to the high relative angular rates that are caused by the canopy's sharp turn.

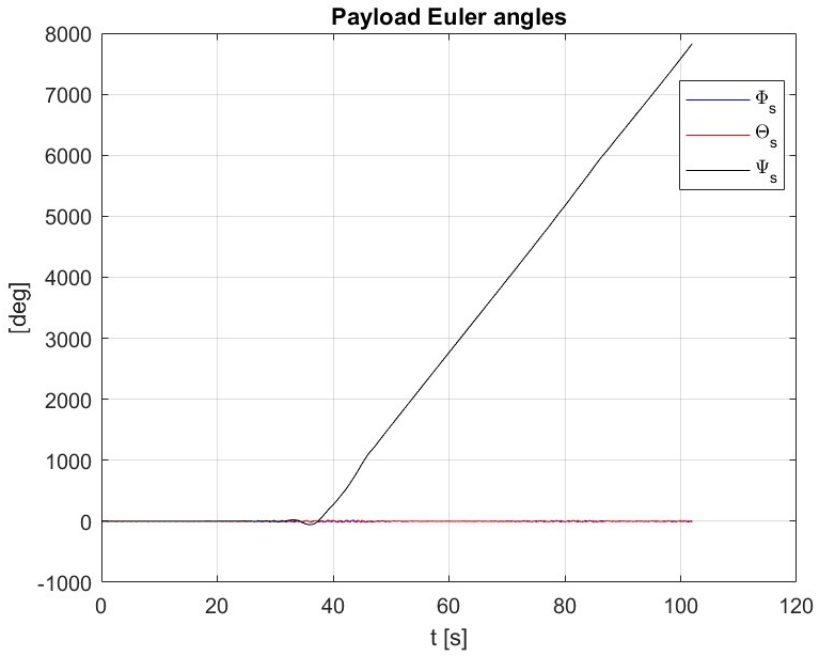

Fig. 21 Payload Euler angles

As seen in Fig. 22 and Fig. 23 the relative angles and angular rates are very high when the canopy turns. It is noticeable that in the middle of the first turn, r increases and remains positive throughout the flight, indicates that the payload keeps rotating in reference to the canopy. This is an important phenomenon, since these type of rotations can be very dangerous for the pilot.

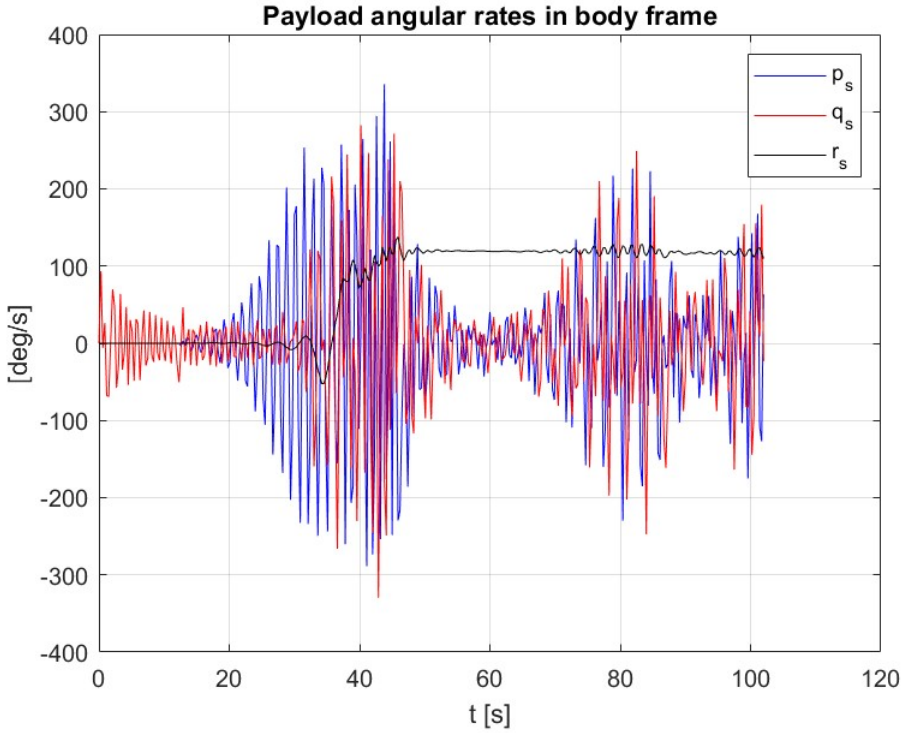

Fig. 22 Payload Angular rates

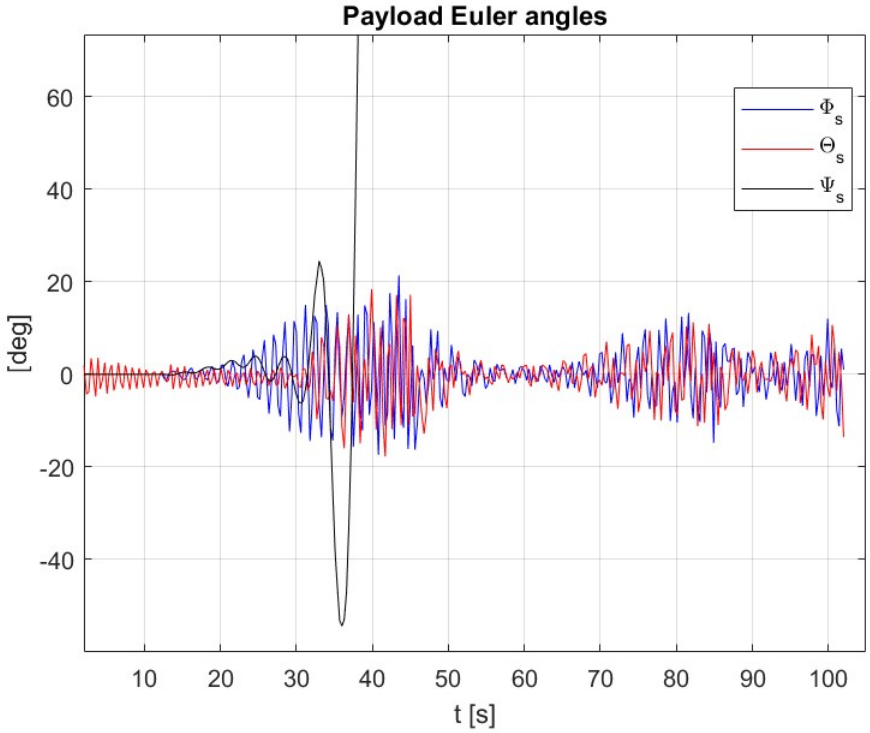

Fig. 23 Payload Euler Angles - Close Up

6 Summary and next steps

In this project, we successfully developed a real-time parafoil piloting simulator by implementing a dynamic model of a RAM Air Parachute. First, we provided an overview of existing simulation methods. We found that the most suitable approach is to formulate the aerodynamic forces analytically using approximated aerodynamic coefficients. Then, we explained in detail the 6-DOF and 9-DOF dynamic models, including definitions of the coordinate systems and rotation matrices, and formulation of the aerodynamic forces and equations of motion. Afterwards, we described the two main parts of the developed simulator - the real-time interface and the simulation backbone, and explained the simulator architecture and how to operate it.

Finally, we analyzed the results of the 6-DOF and 9-DOF simulation and compared them with our expectations and empirical knowledge of canopy pilots. We confirmed that the behavior of the parafoil matched our expectations regarding the parafoil position, orientation, velocity, and angular rates. In addition, we discussed the differences between the 9-DOF and 6-DOF models. We observed that the 9-DOF model is more nuanced, and can account for behaviours that can not be seen in the 6-DOF model, such as coordinated turn and payload rotation. However, the simulated canopy with properties of the small 'SnowFlake' system has a considerably different dynamics relative to sports full-size skydiving canopies. This is particularly seen in the behavior of the pitch angle during the flare maneuver and downward velocity during the turning maneuvers.

Based on the work presented in this report, we suggest the following next steps:

- Further examination of the 6-DOF model with 'SnowFlake' properties to understand the source of the discrepancies found in the canopy behavior relative to empirical expectations based on our acquaintance with the full-size (human-piloted) systems.
- Obtaining/ estimating from experiments the properties of a parafoil relevant to a human pilot. Initial efforts in this direction can be found in [12].
- Validating the simulation by comparing the results to experimental data from real-life parachuting.
- Combining the simulator with a physical interface to simulate real-life steering. A simple yet meaningful laboratory set-up which can be used for this purpose was developed in [13].
- Presenting the simulator output (motion in the inertial space in the "natural" environment) in a Virtual Reality interface, for a better visualization of the canopy flight from the pilot's perspective.

The code for the simulator, along with a short video of a canopy flight from the simulator, is available at: `https://figshare.com/articles/software/Real_time_parachute_simulator_6DOF_zip/26341009`

References

[1] Eslambolchi, A., "COMPUTATION OF FLOW OVER A FULL-SCALE RAM-AIR PARACHUTE CANOPY," 2012.

[2] MehdiGhoreyshi, A. J. A. J. R. M., KeithBergeron, "Computational aerodynamic modeling for flight dynamics simulation of ram-air parachutes," 2015.

[3] Yakimenko, O. A., *Precision Aerial Delivery Systems: Modeling, Dynamics and Control*, Progress in astronautics and aeronautics, Vol. 248, American Institute of Aeronautics and Astronautics, 2015.

[4] Jann, T., "Aerodynamic model identification and GNC design for the parafoil-load system ALEX," 2001.

[5] Gorman, C. M., and Slegers, N. J., "Comparison and Analysis of Multi-body Parafoil Models With Varying Degrees of Freedom," 2011.

[6] Ward, S. C., Michael, and Costello, M., "Parafoil control using payload weight shift," 2014, pp. 204–215.

[7] Sandaruwan Gunasinghe, D. S., GKA Dias, and Weerasinghe, M., "A Real-Time 6DOF Computational Model to Simulate Ram-Air Parachute Dynamics," 2017.

[8] Kemal Güven, A. T. , "Direction Stabilization and Simulation of an Aerial Delivery System with Ram-Air Parachute," 2022. https://doi.org/https://doi.org/10.21203/rs.3.rs-1458039/v1.

[9] Ermolli, L., "Parafoil Control Authority for Landing on Titan," 2016-2017, pp. 13–20.

[10] Lissaman, P., and Brown, G., "Apparent mass effects on parafoil dynamics," *Aerospace Design Conference*, 1993, p. 1236.

[11] "U.S Standard atmosphere," Tech. rep., NASA, 1976. URL ntrs.nasa.gov/citations/19770009539.

[12] Zeev, O. B., "Processing of GPS data collected during maneuvers of RAM-air 135 ft^2 parachute," 2024. URL https://doi.org/10.6084/m9.figshare.25751169.v2.

[13] Osazuwa, E., "Building the Setup for the Canopy Flight Training Simulator: Integrating User Steering Inputs," 2024. URL https://doi.org/10.6084/m9.figshare.26048566.v2.

Appendix

Simulator functions and manual

Real time interface

"simulator" - main function

- Input - canopy properties, initial conditions
- Output - figure presenting real time position and orientation of the canopy in the "natural" environment.

"DrawCanopy"

Builds the simulation environment (Canopy, air bubbles, ground).

- Input - canopy properties, initial canopy position and orientation
- Output - figure presenting the simulator environment.

"keyCallback"

Called when a key is pressed during the simulation. The function dictates how much the toggles are pulled according to the user's key inputs.

- Input - user key input, toggle pull limits
- Output - toggle pull level

"updatePosition"

Samples the backbone of the simulation a few times a second and receives canopy position and orientation. Converts the data into canopy graphic using a separate function, and presents it to the user.

- Input - canopy properties, wind conditions, state vector at the former step, toggle input
- Output - canopy graphics at the next step

"getCorners"

Draws the graphics of the canopy

- Input - canopy position and orientation
- Output - canopy graphics

Simulator backbone

"flight simulation ode" Called by the ODE45 solver, and formulates the equations of motions.

- Input - canopy properties, state vector at former step, steering input, wind conditions

- Output - data id provided to ODE45 solver that numerically propagates the equations of motion and gives the state vector at the next step

"aerodynamic forces"

Calculates the aerodynamic forces and moments acting on the canopy based on Eq. (13), Eq. (14).

- Input - canopy properties, state vector at former step, steering input, wind conditions
- Output - aerodynamic forces and moments

"gravity force"

Calculates the gravity force acting on the canopy base on the equations in Eq. (9).

- Input - canopy properties, state vector at former step
- Output - gravity force

"atm model"

Basic atmospheric model as explained in detail in 3.4

- Input - height
- Output - air density

Manual

The simulator begins by starting the main function "simulator". The user can control the canopy using the keyboard: "P" pulls the right toggle and "O" releases it, "W" pulls the left toggle and "E" releases it. In addition, the user can press "X" to zoom in and "Z" to zoom out.

The user cannot exceed the allowed level of toggle input specified by the canopy properties, however, it is possible for the canopy to stall during the flight as a result of aggressive steering. In that case, the simulation will automatically stop within a few seconds. The simulation will also end automatically if the user exits the "natural" environment initially drawn. In any time, the user can press "S" to stop the simulation. When the simulation stops, either automatically or by the user, the user is presented with the flight data, including canopy flight path, canopy position and orientation, velocity in body frame and in the inertial frame, angular rates and input history.